

The $H\alpha$ luminosity function and star formation rate up to $z \sim 1^*$

L. Tresse,^{1†} S. J. Maddox,² O. Le Fèvre¹ and J.-G. Cuby³

¹Laboratoire d'Astrophysique de Marseille, Les Trois-Lucs, B.P. 8, 13376, Marseille Cedex 12, France

²School of Physics and Astronomy, University of Nottingham, Nottingham, NG7 2RD

³ESO, Alonso de Cordova 3107, Vitacura, Casilla 19001, Santiago 19, Chile

Accepted ---. Received ---; in original form ---

ABSTRACT

We describe ISAAC/ESO-VLT observations of the $H\alpha$ $\lambda 6563$ Balmer line of 33 field galaxies from the Canada-France Redshift Survey (CFRS) with redshifts selected between 0.5 and 1.1. We detect $H\alpha$ in emission in 30 galaxies and compare the properties of this sample with the low-redshift sample of CFRS galaxies at $z \sim 0.2$ (Tresse & Maddox 1998). We find that the $H\alpha$ luminosity, $L(H\alpha)$, is tightly correlated to $M(B_{AB})$ in the same way for both the low- and high-redshift samples. $L(H\alpha)$ is also correlated to $L([O\ II]\lambda 3727)$, and again the relation appears to be similar at low and high redshifts. The ratio $L([O\ II])/L(H\alpha)$ decreases for brighter galaxies by as much as a factor 2 on average. Derived from the $H\alpha$ luminosity function, the comoving $H\alpha$ luminosity density increases by a factor 12 from $\langle z \rangle = 0.2$ to $\langle z \rangle = 1.3$. Our results confirm a strong rise of the star formation rate (SFR) at $z < 1.3$, proportional to $(1+z)^{4.1 \pm 0.3}$ (with $H_0 = 50 \text{ km s}^{-1} \text{ Mpc}^{-1}$, $q_0 = 0.5$). We find an average $\text{SFR}(2800\text{\AA})/\text{SFR}(H\alpha)$ ratio of 3.2 using the Kennicutt (1998) SFR transformations. This corresponds to the dust correction that is required to make the near UV data consistent with the reddening-corrected $H\alpha$ data within the self-contained, I -selected CFRS sample.

Key words: surveys - galaxies: evolution - galaxies: starburst - galaxies: luminosity function, mass function

1 INTRODUCTION

Measuring the comoving space density of the star formation rate (SFR) as a function of cosmic epoch has advanced rapidly over the last few years, it has set important constraints on our knowledge of galaxy formation and evolution. Since the major work of Madau et al. (1996) using the Canada-France Redshift Survey (CFRS) data at $z < 1$ (Lilly et al. 1996) and the Lyman-break galaxy population at $z > 2$ (Steidel et al. 1996), many observational studies and detailed models have emerged to trace back the SFR history.

The SFR density is usually derived from the mean luminosity density, that is $\mathcal{L} = \int_0^\infty \phi(L)LdL = \phi^*L^*\Gamma(\alpha + 2)$, assuming galaxies follow a Schechter (1976) luminosity function with a characteristic luminosity, L^* , a faint-end slope, α , and a normalization density parameter, ϕ^* . The faint-end slope is found to be greater than -2 , implying a high-space density of low-luminosity galaxies, but although

they are very numerous, they contribute little to the mean luminosity density. However as the three Schechter parameters are highly correlated, it is necessary to build the luminosity function over the largest possible range of luminosities. At first sight the SFR density appears a simple and useful tool to trace back the evolution of star formation and link it with the evolution of mass, but discrepancies between different measurements have led to controversy. Uncertainties in the conversion factors from luminosity to star formation rate, coupled with the different survey selection criteria mean that the SFR history of the Universe is still poorly determined, and thus hotly debated. The discrepancies are partly due to the difficulty in relating what we observe to the intrinsic physical and chemical properties of galaxies. Each SFR indicator has pros and cons in the sense that they are more or less dependent on the star formation, and more or less affected by factors other than star formation. Another difficulty is the small number of galaxies in some samples; this leads to large statistical uncertainties, because they do not represent a fair sample of the galaxy population as a whole.

Large and deep galaxy surveys provide estimates of the continuum luminosity density in different rest-frame wave-

* Based on data obtained at the European Southern Observatory on Paranal, Chile.

† Email: laurence.tresse@oamp.fr

length ranges from the far ultraviolet to the far infrared. As well as continuum luminosity density measurements, SFR indicators using line-emission measurements have also been studied, further complicating the picture but stimulating work for a better understanding of the physical star formation processes within galaxies. Observationally speaking, it is generally accepted that the SFR density rises from $z = 0$ to $z \sim 1$, but at higher redshifts it is still unclear whether the SFR density reaches a plateau, or decreases, or increases slowly. There has also been some controversy about the rise at $z < 1$; Lilly et al. (1996) found a steep rise of the 2800-Å luminosity density proportional to $(1+z)^{3.90 \pm 0.75}$, while Cowie, Songaila & Barger (1999) argue for a shallow rise of the 2500-Å luminosity density proportional to $(1+z)^{1.5}$.

In this present study, we investigate the $H\alpha$ $\lambda 6563$ luminosity density evolution using data acquired at the ESO-VLT with the ISAAC infrared spectro-imager (Cuby et al. 2000, Moorwood et al. 1999) mounted at the Nasmyth focus of the first of the four 8.2m VLT Unit Telescopes. We recall that $H\alpha$ luminosities are excellent tracers of instantaneous star formation within galaxies since they are directly proportional to the ionizing UV stellar spectra at $\lambda < 912$ Å. It suffers from stellar absorption and dust attenuation, but dust affects $H\alpha$ at a lower level than the UV, and can be mitigated by reddening correction. Moreover new models (see e.g. Charlot & Longhetti 2001) derive SFR estimates in a self-consistent way accounting for the depletion of heavy elements onto dust grains, for the absorption of ionizing photons by dust in H II regions, and for contamination of Balmer emission by stellar absorption. With these corrections and with the help of several spectral lines, the SFR from $H\alpha$ becomes compatible with the SFR using far-infrared estimators (Charlot et al. 2002). Furthermore, $H\alpha$ is a particularly useful SFR indicator at high redshift since it is directly comparable to low redshift surveys, which makes it straightforward to probe evolution. We concentrate on $H\alpha$ measurements of CFRS galaxies between $0 < z < 1.1$ using the data from Tresse & Maddox (1998) at $z \leq 0.3$, and new $H\alpha$ data at $0.5 < z < 1.1$ taken with the ISAAC spectrograph. These data allow us to quantify for the first time the $H\alpha$ luminosity function and density evolution up to $z \sim 1$ within a single survey. In Section 2 we present our data samples. Section 3 details the ISAAC spectroscopic acquisition, reduction and flux measurements. Section 4 discusses the reddening correction on our measurements. Section 5 presents the $[O II]/H\alpha$ ratio and other properties of the samples. We estimate the SFR density for our samples in Section 6, and conclude with a discussion of our results in Section 7. Throughout this paper, we use $H_0 = 50 \text{ km s}^{-1} \text{ Mpc}^{-1}$ and $q_0 = 0.5$ mainly for ease of comparison with published results.

2 GALAXY SELECTION

Our sample of galaxies is taken from the *I*-band-selected CFRS, of which 591 galaxies have reliable redshifts $0 < z < 1.3$ and apparent magnitudes $17.5 \leq I_{AB} \leq 22.5$, in five regions of the sky (see Le Fèvre et al. 1995). As described below, our sample is made of the low- z sample of $H\alpha$ emitters at $z \leq 0.3$ observed in the five CFRS fields and of the high- z sample of $H\alpha$ emitters at $0.50 < z < 1.05$ observed in three CFRS fields. This offers the opportunity of

direct measurements of evolution within a single survey with a well-controlled selection. Moreover this study does not suffer from uncertainties in line identification as encountered by narrow-band filter surveys.

The CFRS spectral range is 4500–8500 Å, thus the $[O II]\lambda 3727$ line is observable for all galaxies with $z \gtrsim 0.2$, and the $H\alpha$ line is observable only for galaxies at $z \lesssim 0.3$. Our low- z sample consists of 110 out of the 138 CFRS galaxies to $z = 0.3$. They have $H\alpha$ -emission fluxes measured from the original CFRS spectra. This sample was analysed by Tresse & Maddox (1998), who describe the sample in more detail. With new near infrared capabilities we can now measure $H\alpha$ at higher redshifts, and we have focused on CFRS galaxies at $z > 0.5$. For our new observations, we used the ISAAC spectrograph in the short-wavelength mode; this configuration enables us to span the wavelength range 0.9–2.5 μm . The *SZ*- and *J*-band filters with an atmospheric transmission above 0.5 cover the wavelength range 0.98–1.35 μm . Thus $H\alpha$ will be in this range for galaxies within the redshift interval 0.50–1.05. The CFRS contains 323 galaxies in this interval.

For our high- z sample, we selected our targets using the following two well-defined criteria chosen so that we could measure $H\alpha$ -emission fluxes as accurately as possible. The first criterion was aimed at maximizing the probability of detecting $H\alpha$ in emission. In nearby samples, the $[O II]$ and $H\alpha$ emission lines are correlated, even though there is a large dispersion (see e.g. Kennicutt 1992, Tresse et al. 1999). Thus we selected galaxies where the CFRS spectra show $[O II]$ emission with observed equivalent width $EW \gtrsim 10$ Å. There are 251 targets out of 323 with $EW([O II]) \gtrsim 10$ Å. The second criterion was to select galaxies with $H\alpha$ redshifted away from strong OH night-sky emission lines. For each of the $EW([O II]) \gtrsim 10$ Å targets we cross-correlated the expected redshifted wavelength of $H\alpha$ with a list of OH-sky lines, and rejected galaxies where $H\alpha$ would be too close to a sky line. For the galaxy line-widths we assumed $FWHM(H\alpha) = 13.1 \times (1+z)$ Å, corresponding to a rotation speed of 600 km s^{-1} , and for the OH-sky lines we assumed $FWHM \sim 8$ Å, corresponding to the instrumental resolution for our observing set-up. These FWHM are large enough so we could be fairly confident that the observed $H\alpha$ will be in between the OH bands, even with the uncertainty from the redshift measurement. Rejecting the galaxies at redshifts where $H\alpha$ is likely to be affected by a sky line, leaves 84 targets.

3 ISAAC SPECTROSCOPY

3.1 Observations

Our spectroscopic observations were done in service mode during Period-63 and Period-64 with the ISAAC spectrograph at the ESO-VLT. Spectra were taken at Medium Resolution, and with the Short-Wavelength channel equipped with a 1024×1024 Hawaii Rockwell array. The pixel scale is 0.147 arcsec per pixel. We opted for long slits of 2 arcsec width, ensuring that most of the light of the target was in the slit (see the 5×5 arcsec² postage stamps from HST data shown in Fig. 1 of Schade et al. 1995). This set-up gives a resolution of $R \simeq 1500$, and covers a wavelength range

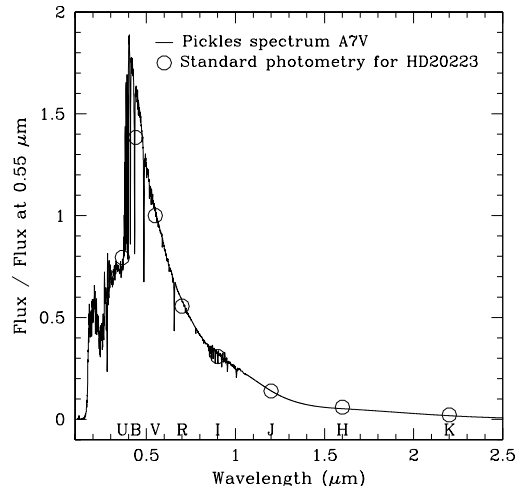


Figure 1. Broad-band photometry (open points) and the inferred spectrum for the standard star HD20223. The spectrum is for an A7V star taken from the Pickles (1998) library, normalized to the observed photometry for HD20223. The agreement between the photometry and spectral flux is excellent in all bands, including J, H and K.

of $0.16 \mu\text{m}$ in the *SZ* filter, and $0.29 \mu\text{m}$ in the *J* filter. We chose six central wavelengths which are away from the strongest OH bands and cover the wavelength range for the expected positions of $H\alpha$ for all the target galaxies. The central wavelengths are 1.02 and $1.06 \mu\text{m}$ for the *SZ* filter, 1.11 , 1.18 , 1.26 and $1.33 \mu\text{m}$ for the *J* filter. For each observation, the appropriate central wavelength was selected according to the redshift of the target. Since the observations were carried out in service mode, the choice of integration time had to be made before-hand. We set them by comparing to the commissioning data which were available at that time, and adjusting the time for each galaxy according to its [O II] flux and the spectral type. Thus the individual integration times (called DIT) were set to be either 600s, 900s or 1200s. During the observations the telescope was nodded between A and B positions, 20 arcsec apart along the slit. The total integration time was $2 \times \text{DIT}$, consisting of one sequence AB. Dark frames, flat-fields and (Xe+Ar) arc lamp spectra were taken with the same filter, central wavelength and slit width for each of the targets observed during the night. In total, 33 observation blocks (OB) were observed. Table 3.2 lists the target name, the exposure time and the filter used for each OB.

3.2 Reduction and calibration

We used the *IRAF/CL* package for our data reduction. We first subtracted the dark image from the A, B and flat images. Next we divided the A and B images by the flat response. The resulting A and B images were then subtracted from each other to form (A–B) and (B–A) images. At this stage, the images have been corrected for the dark current, bias level and flat-field, and have been sky subtracted. To combine A and B data, we first apply a spatial offset to the (B–A) image, equal to the nod between the A and B positions so that the galaxy signal appears at the same position

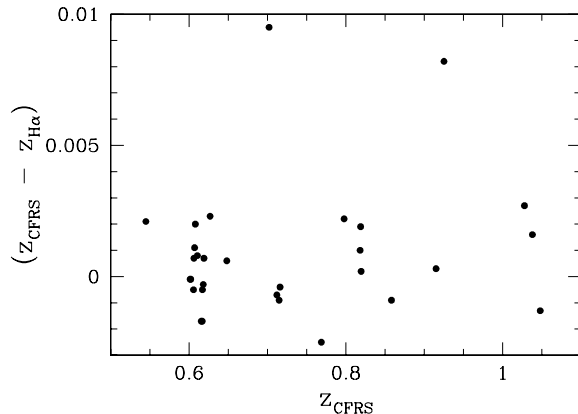


Figure 3. Difference in redshift between those measured from the original CFRS optical spectra, z_{CFRS} , and those from our $H\alpha$ line observed in the near infrared, $z_{H\alpha}$. The *rms* is 0.0025, or 0.0014 when excluding the two most discrepant values.

in each image. Then we average the (A–B) image and the offset (B–A) image after rejecting 3σ discrepant pixels. This procedure removes most cosmic rays, sky residuals and bad pixels. Then a 1D spectrum was extracted at the position of the emission line, and calibrated in wavelength using the arc lines.

Finally the 1D spectra were spectrophotometrically calibrated with a standard star observed with the same setup as the target. For most galaxies the standard star observations were taken during the same night. For 2 galaxies, standard stars from neighbouring nights were used. At the time of our observations, carefully flux calibrated standard star spectra covering the near infrared bands did not exist, and the only information we had for the standard stars was the spectral type and the magnitude in several pass bands. Therefore to determine the spectral response function we compared the observed stellar spectra to spectra from the Pickles (1998) stellar library of composite spectra. As a check on the reliability of the Pickles flux calibration, we compared the spectra to the broad-band magnitudes. We found that the agreement between the spectral shape and the UBVRJHK magnitudes is excellent as shown for an example in Fig. 1.

3.3 Emission-line measurements

We measured the integrated fluxes and the corresponding 1σ errors using the package *SPLIT* under *IRAF/CL*, interactively marking two endpoints around the line to be measured. This method allows the accurate measurement of lines which are not well fit by simple Gaussian profiles, including lines with asymmetric shapes. Out of 33 observation blocks, we obtained 30 $H\alpha$ flux measurements. The spectra are shown in Fig. 2, and the fluxes are presented in Table 3.2. We detect no emission line in the remaining 3 observations; for these either $H\alpha$ is below our detection limit, or it falls on an OH line due to a large error in the redshift measurement. Discrepancies between the redshifts measured from the original CFRS spectra and from ours are less than 0.003, except for two cases (0.0095 and 0.0082 respectively for #03.0984 and

Table 1. Data for the 33 observed galaxies with the ISAAC spectrograph at ESO-VLT.

CFRS Id. ^a	z ^b	Note ^c	I _{AB} ^d	(V-I) _{AB} ^d	M(B _{AB}) ^e	EW([O II]) ^f	flux([O II]) ^g	EW(H α) ^f	flux(H α) ^g	A ^h	DIT ⁱ	Filter ^j	Morphology ^k
00.0338	1.0279	8	22.37	0.29	-21.23	104.19 \pm 15.16	11.39 \pm 1.17	57.56 \pm 27.64	17.85 \pm 3.11	11	600	J	-
00.0564	0.6105	3	22.12	1.63	-20.05	16.14 \pm 3.33	3.01 \pm 0.60	11.80 \pm 4.82	14.03 \pm 3.90	20	1200	SZ	-
00.0874	0.7119	2	22.37	1.44	-20.27	21.40 \pm 4.88	2.23 \pm 0.47	8.91 \pm 5.85	6.45 \pm 2.85	13	1200	J	-
00.1825	1.0390	9	22.07	1.68	-21.80	47.38 \pm 12.46	5.49 \pm 1.05	-	-	-	1200	J	-
03.0133	1.0480	9	22.45	1.00	-21.35	64.53 \pm 21.09	4.67 \pm 1.11	-	-	-	900	J	-
03.0145	0.6052	4	21.57	0.99	-20.80	32.79 \pm 3.54	12.02 \pm 1.17	-	-	-	600	SZ	-
03.0167	0.6020	4	20.67	1.54	-21.49	7.78 \pm 1.97	5.73 \pm 1.44	12.86 \pm 8.28	7.13 \pm 2.26	19	1200	SZ	-
03.0422	0.7148	3	21.21	1.38	-21.45	10.11 \pm 3.27	5.01 \pm 1.60	117.20 \pm 249.59	26.56 \pm 13.90	26	1200	J	-
03.0480	0.6079	3	22.12	0.87	-20.31	89.87 \pm 24.34	15.56 \pm 3.23	21.09 \pm 13.07	23.85 \pm 7.23	23	600	SZ	Sab
03.0485	0.6056	4	22.22	0.77	-20.24	80.67 \pm 2.83	24.97 \pm 0.62	140.35 \pm 84.25	82.32 \pm 10.68	18	600	SZ	Irr
03.0488	0.6069	4	21.58	0.87	-20.85	66.56 \pm 5.78	27.82 \pm 2.03	38.04 \pm 10.88	45.05 \pm 5.22	19	600	SZ	Irr
03.0570	0.6480	3	22.07	1.21	-20.38	28.11 \pm 2.75	9.40 \pm 0.87	32.88 \pm 23.33	22.07 \pm 5.79	8	600	SZ	-
03.0589	0.7160	3	22.18	1.37	-20.48	22.45 \pm 3.95	5.70 \pm 0.96	43.88 \pm 46.49	22.89 \pm 8.78	15	1200	J	-
03.0595	0.6061	4	21.46	1.33	-20.78	18.33 \pm 3.51	5.44 \pm 1.00	10.66 \pm 3.76	26.94 \pm 7.02	19	1200	SZ	Merger/Irr
03.0615	1.0480	9	22.01	0.96	-21.78	30.25 \pm 3.60	8.81 \pm 0.95	53.24 \pm 75.59	13.91 \pm 5.80	17	600	J	-
03.0879	0.6013	2	22.48	0.96	-19.89	28.87 \pm 6.51	4.11 \pm 0.85	12.42 \pm 29.24	5.94 \pm 5.92	20	600	SZ	-
03.0952	0.8581	3	22.49	0.99	-20.66	34.59 \pm 3.76	5.81 \pm 0.57	93.52 \pm 153.54	7.60 \pm 3.17	15	900	J	-
03.0984	0.7020	3	19.29	0.93	-23.43	5.26 \pm 3.08	2.04 \pm 1.19	2.66 \pm 1.21	14.45 \pm 6.01	15	600	J	-
03.1027	1.0380	9	22.32	1.79	-21.55	56.98 \pm 5.71	10.62 \pm 0.83	101.85 \pm 164.02	16.44 \pm 6.95	36	900	J	Merger/Sab
03.1032	0.6180	4	20.49	1.94	-21.63	9.91 \pm 2.15	8.41 \pm 1.80	0.83 \pm 0.30	4.46 \pm 1.52	19	1200	SZ	E/S0
03.1242	0.7687	3	21.69	1.03	-21.21	27.47 \pm 3.01	6.69 \pm 0.68	114.17 \pm 345.23	21.43 \pm 21.72	18	600	J	-
03.1309	0.6170	4	20.62	1.08	-21.76	22.58 \pm 3.35	10.41 \pm 1.50	18.92 \pm 6.75	36.41 \pm 8.46	22	600	SZ	-
03.1345	0.6167	3	21.43	1.65	-20.75	17.43 \pm 3.38	7.00 \pm 1.33	22.89 \pm 5.83	12.19 \pm 2.23	20	900	SZ	-
03.1349	0.6155	4	20.87	1.29	-21.42	22.02 \pm 2.83	12.86 \pm 1.46	27.46 \pm 3.59	25.52 \pm 2.39	20	900	SZ	-
03.1534	0.7977	8	22.45	0.70	-20.58	45.01 \pm 5.23	12.79 \pm 1.30	72.33 \pm 179.12	12.81 \pm 7.42	11	600	J	-
03.9003	0.6189	4	20.77	1.35	-21.51	30.64 \pm 3.21	18.77 \pm 1.86	134.69 \pm 113.57	56.41 \pm 12.30	21	600	SZ	Scd/Irr
22.0429	0.6267	4	21.95	1.59	-20.29	24.25 \pm 2.10	6.53 \pm 0.50	13.38 \pm 2.53	26.12 \pm 4.01	15	1200	SZ	-
22.0637	0.5448	4	20.79	1.11	-21.26	37.36 \pm 5.19	15.16 \pm 1.93	96.28 \pm 86.74	55.48 \pm 14.13	32	600	SZ	-
22.0764	0.8194	3	22.20	1.29	-20.81	17.35 \pm 2.98	5.13 \pm 0.85	7.21 \pm 1.31	11.87 \pm 1.87	22	1200	J	Irr
22.0770	0.8188	4	21.78	1.58	-21.21	36.22 \pm 3.80	10.04 \pm 0.91	68.96 \pm 51.07	20.67 \pm 5.25	16	900	J	-
22.0779	0.9252	3	21.86	1.05	-21.50	10.23 \pm 1.44	3.86 \pm 0.51	6.48 \pm 2.86	6.96 \pm 2.30	20	600	J	Sa/Sab
22.0843	0.9150	9	22.10	0.85	-21.22	14.86 \pm 4.76	3.70 \pm 1.13	24.03 \pm 10.34	17.06 \pm 4.78	20	600	J	-
22.1406	0.8182	4	22.16	1.16	-20.87	57.01 \pm 5.26	17.51 \pm 1.28	57.62 \pm 24.93	33.35 \pm 5.40	18	600	J	Comp/Sab

^a Identification number from the CFRS catalogue.^b Redshift from CFRS spectroscopic observations.^c Confidence class of CFRS redshift measurements (4, 3 and 2: 100%, 95% and 85% confidence levels, 8 & 9: single emission-line spectrum).^d Apparent magnitudes from the CFRS photometry.^e Absolute rest-frame *B*-band magnitude.^f Rest-frame equivalent width in Å ([O II] from CFRS spectra, H α from our ISAAC spectra.)^g Line flux in units of 10⁻¹⁷ erg cm⁻² s⁻¹ ([O II] from CFRS spectra, H α from our ISAAC spectra.)^h Aperture in pixels (0.147 arcsec per pixel) for extracting both 1D object and sky spectra.ⁱ For the ISAAC observations DIT is the integration time in *s* at each nod position (AB), so the total integration time is 2×DIT (see Section 3.1).

For three galaxies observed during commissioning data, different procedures were followed:

#03.0952: 1 hr exposure ABBA sequence, offset 10 arcsec, dispersion of 0.595 Å/pixel, long slit of 2 arcsec width;

#03.1345 & #03.1349: 1 hr exposure, ABBA sequence, offset 20 arcsec, dispersion of 0.458 Å/pixel, long slit of 2 arcsec width.

^j Filter used for our ISAAC observations.^k HST morphological type (see Brinchmann et al. 1998).

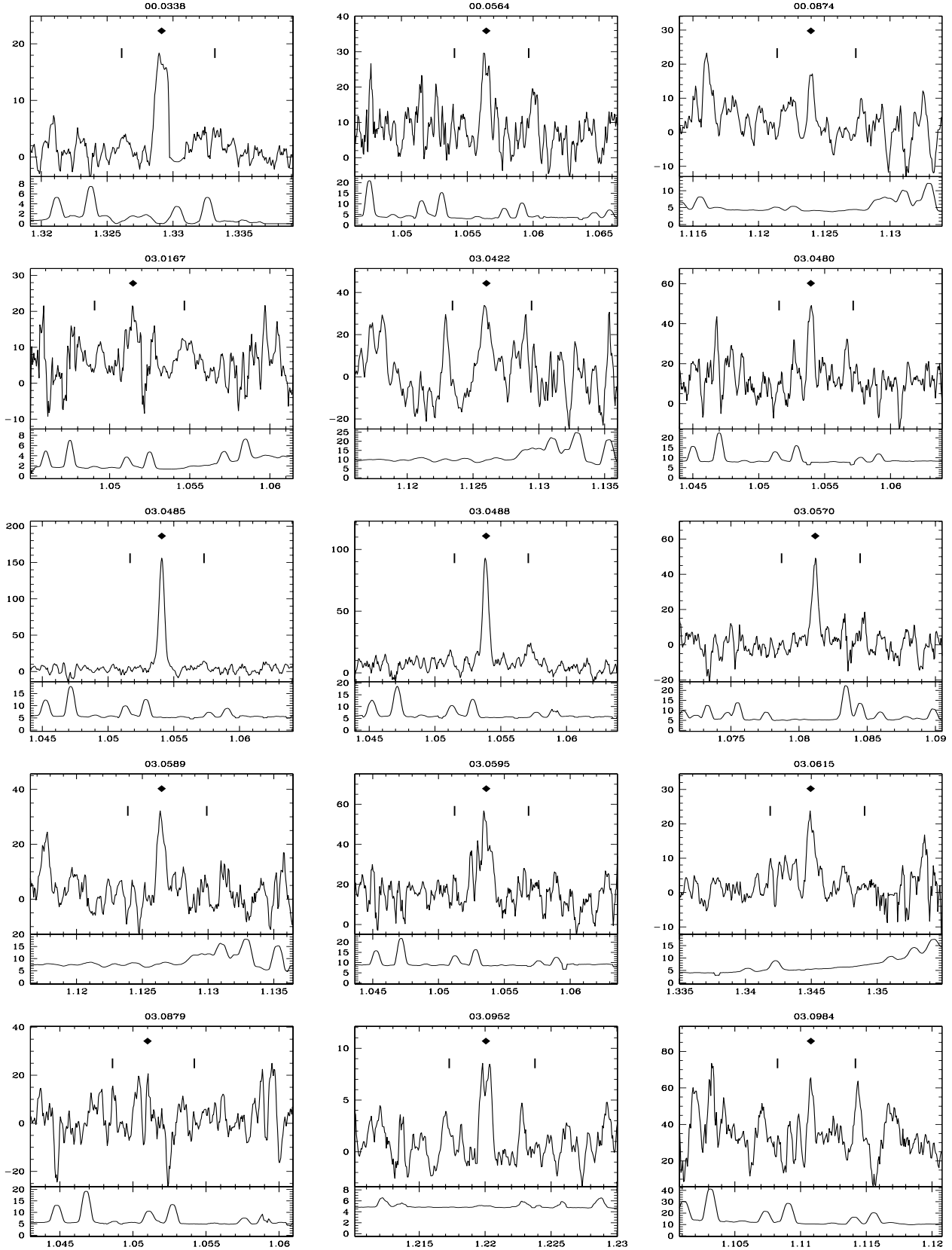


Figure 2. The 30 $H\alpha$ emission-line observed-frame spectra between $z = 0.5$ and 1.1 , observed with the ISAAC spectrograph at the ESO-VLT (top panel). In the plot, the spectra have been smoothed using a 7 pixel boxcar filter, the X-axis is the observed wavelength in μm , the Y-axis is the flux in units of $10^{-18} \text{ erg s}^{-1} \text{ cm}^{-2}$, the diamond indicates the position of the detected $H\alpha$ $\lambda 6563$ line, the vertical bars indicate the positions of the $[\text{N II}]\lambda 6548$ and $[\text{N II}]\lambda 6583$ lines. The sky noise level is shown in the bottom panel. In each case, both the object and the sky have been extracted with the same aperture. The CFRS identification is written at the top of each window (see also Table 3.2).

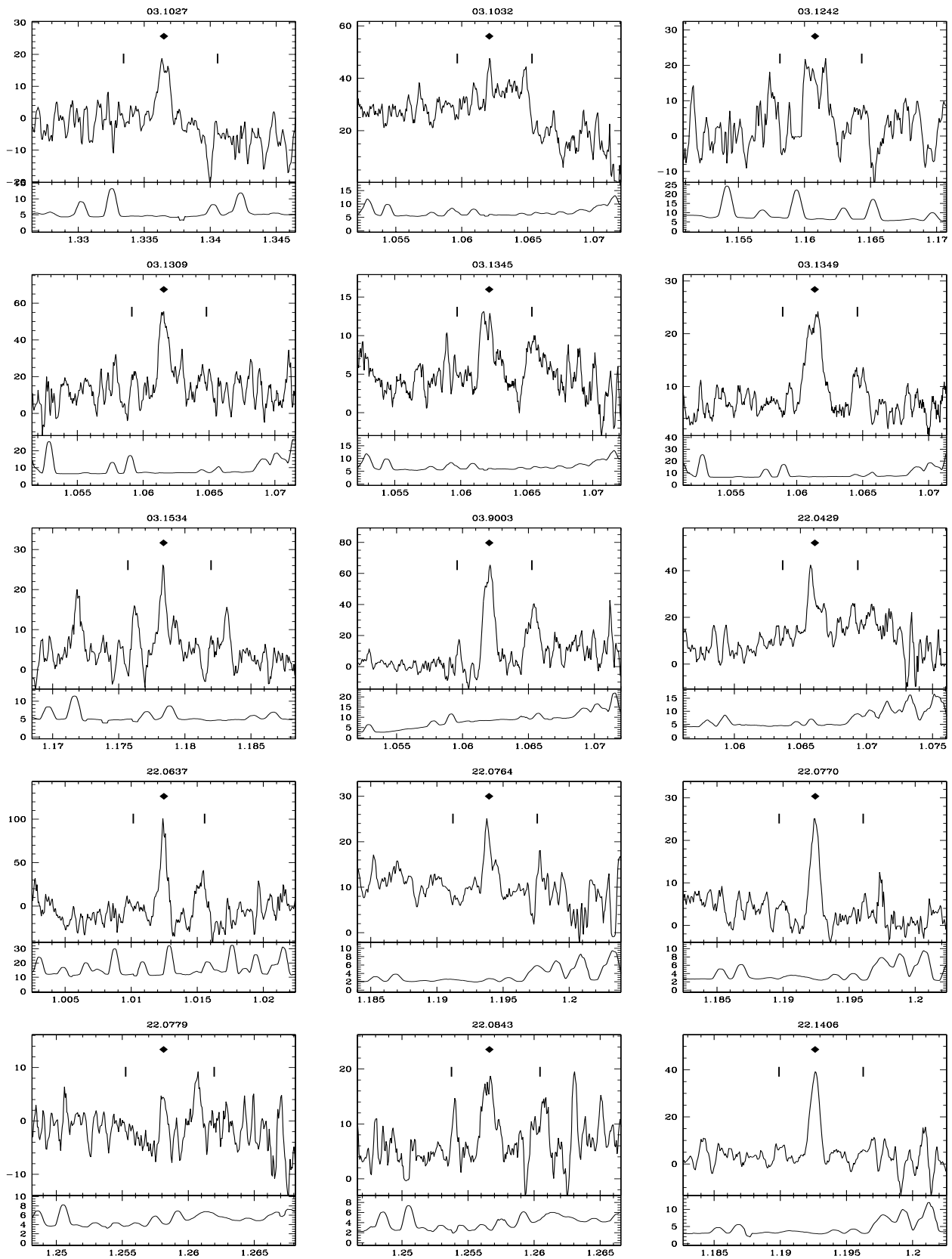


Figure 2. Suite.

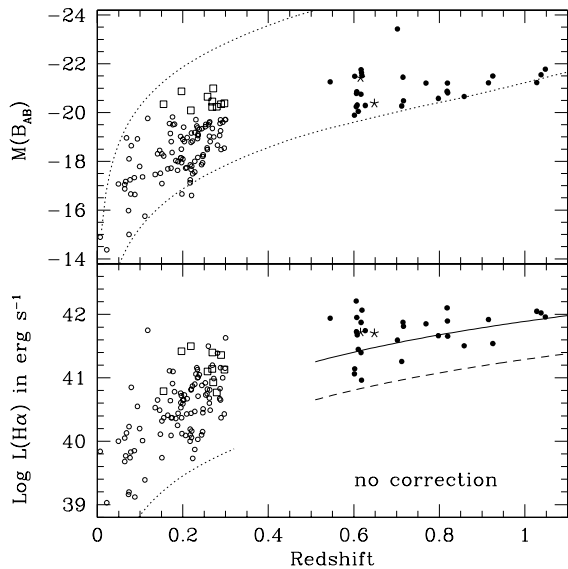


Figure 4. $M(B_{AB})$ and $\log L(H\alpha)$ versus redshift for galaxies at $z \leq 0.3$ (110 open symbols; Tresse & Maddox 1998), and at $z > 0.5$ (30 solid and starred symbols; this work). Low- z galaxies with $M(B_{AB}) < -20$ mag are plotted as open squares (10 out of 110). In this figure, no reddening correction has been applied to the $H\alpha$ luminosities; they are derived directly from observed $H\alpha$ fluxes. In the following figures, all but two of the high- z galaxies are corrected for reddening by assuming $A_V = 1$ (solid dots). For the two galaxies shown by starred symbols we estimate the reddening from the Balmer decrement (see Section 4). In the top panel, the dotted lines show the I_{AB} CFRS apparent magnitude limits converted to $M(B_{AB})$ assuming the spectral energy distribution is like an Sab galaxy. In the bottom panel, the dotted line shows the survey detection limit for an emission line observed in the I -band at the $I_{AB} = 22.5$ mag limit, and with observed $EW = 10$ Å. The dashed line shows the limit for 22 Å assuming $I_{AB} = J$, and the solid line shows the limit for 22 Å assuming $(I_{AB} - J) = 1.5$, as discussed in Section 5.1.

#22.0779, see Fig. 3) for which the CFRS calibration appears less accurate. Excluding these cases, the *rms* discrepancy is 0.0014, i.e. 420 km s^{-1} , consistent with the redshift accuracy of $350\text{--}550 \text{ km s}^{-1}$ estimated in Le Fèvre et al. (1995). The high-resolution of our spectra means that $H\alpha$ is well separated from the $[N \text{ II}]\lambda\lambda 6548, 6583$ lines which are detected in several spectra. Since the slit is 2 arcsec wide, it covers most of the apparent size of galaxies at $z > 0.5$ (see the $5 \times 5 \text{ arcsec}^2$ postage stamps from HST data shown in Fig. 1 of Schade et al. 1995). Thus we did not apply any aperture correction to our measurements. Line luminosities are given in erg s^{-1} by,

$$L = 4\pi(3.086 \cdot 10^{24} d_L)^2 f,$$

where f is the integrated line flux in $\text{erg s}^{-1} \text{ cm}^{-2}$, and d_L is the luminosity distance in Mpc. In the case of $H\alpha$, the line fluxes vary from 5 to $82 \cdot 10^{-17} \text{ erg s}^{-1} \text{ cm}^{-2}$, with an average flux of $22 \cdot 10^{-17} \text{ erg s}^{-1} \text{ cm}^{-2}$.

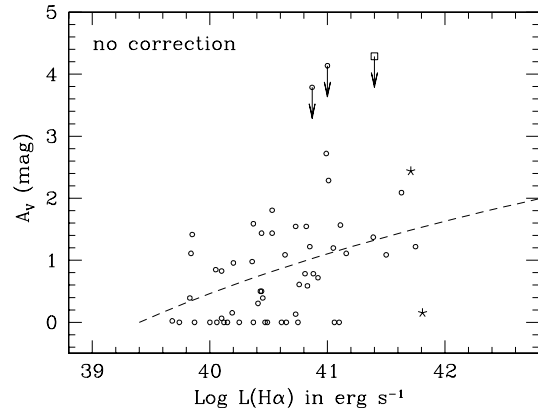


Figure 5. A_V versus $\log L(H\alpha)$ for our galaxies for which we could measure a Balmer decrement. No reddening correction has been applied to the $H\alpha$ luminosities. The different symbols are defined in Fig. 4. The dashed line shows the relation derived from the relation $H\alpha/H\beta = 0.82 \log(L(H\alpha) 10^{-41.09}) + 4.24$ from Sullivan et al. (2001), using $H\alpha/H\beta = 2.86 \cdot 10^{0.323C}$ and $A_V = C \cdot 3.2/1.47$. See Section 4.

4 REDDENING CORRECTION

Reddening is produced by interstellar extinction along the line of sight to each observed galaxy. Interstellar extinction due to our Galaxy is small ($A_V \lesssim 0.1$ mag), because the CFRS fields are located at high galactic latitude ($|b_{\text{II}}| \geq 45^\circ$); hence most of the reddening is intrinsic to the observed galaxy. For about two thirds of the galaxies, the $H\beta$ lines observed in the CFRS spectra have too low signal-to-noise to be accurately measured, so we cannot estimate A_V for every galaxy. Thus we present our results using two approaches: (a) with no correction for reddening, (b) with a reddening correction derived from two observed Balmer lines, and if not observed assuming an average correction A_V of 1 mag as found in several nearby samples (e.g. for instance Kennicutt 1992, Tresse & Maddox 1998). Note that in all of these cases the estimates refer only to reddening that occurs after the emission of the Balmer photons, and they do not account for any obscuration of Lyman continuum photons before this. Charlot et al. (2002) suggest that the absorption of Lyman continuum may introduce a further attenuation of $\sim 20\%$.

For $z > 0.5$ galaxies we assume $A_V = CR/1.47 \simeq 1$ mag ($R = 3.2$; Seaton 1979), which corresponds to an extinction correction of $C = 0.45$. Hence fluxes are dereddened as $f(H\alpha)10^{0.677C}$, and $f([O \text{ II}])10^{1.2553C}$ using the galactic extinction law from Seaton (1979). We note that Hammer et al. (2000) estimated the $f(H\beta)/f(H\gamma)$ ratio using high-resolution spectra of two of our $z > 0.5$ targets; the ratios are 2.18 for #03.0570 and 2.98 for #03.1349. These ratios correspond to A_V of 0.15 and 2.44 mag respectively, or $C = 0.07$ and 1.12 respectively, derived using $I_0(H\gamma/H\beta) = 0.468$ for case B recombination with a density of 100 cm^{-3} and a temperature of 10,000 K (Osterbrock 1989), and applying Seaton's law, $f(H\gamma/H\beta) = I_0(H\gamma/H\beta)10^{0.129C}$. These two galaxies are plotted as starred symbols in the figures. For the $z \leq 0.3$ galaxies, as described in Tresse & Maddox (1998), for half of the sample, we derived C using measured $f(H\alpha)/f(H\beta)$ ratios and the same prescription as earlier

with $f(\text{H}\alpha/\text{H}\beta) = I_0(\text{H}\alpha/\text{H}\beta)10^{0.323C}$, ($I_0(\text{H}\alpha/\text{H}\beta) = 2.86$; Osterbrock 1989). For the remaining half we used $A_V = 1$ mag.

Although we use an average reddening correction, the true A_V varies significantly from galaxy to galaxy. For instance, in our CFRS low- z spectra where the $\text{H}\beta$ lines have sufficient signal-to-noise, we find values ranging from about 0 to 2 mag as shown in Fig. 5. Variations in stellar absorption introduce some scatter in apparent reddening, but most of the scatter represents genuine differences in reddening. Ideally $\text{H}\alpha$ and $\text{H}\beta$ should be corrected for stellar absorption, but this is not possible with the CFRS spectra. For galaxies without high signal-to-noise spectra covering both $\text{H}\alpha$ and $\text{H}\beta$ we can do no better than assume a constant $A_V = 1$ mag as found in several nearby samples. This applies to all, except two, of our high- z galaxies, and half of our low- z sample. Although not ideal, this simple approximation should be correct on average, and allows us to examine some of the effects of reddening on our results. We note that Fig. 5 shows that our measured A_V increases towards high $\text{H}\alpha$ luminosities, and thus towards bright B -band luminosities (see Fig. 6). UV -selected galaxy samples show a similar trend (Sullivan et al. 2001), as do samples using FIR data (for instance e.g. Wang & Heckman 1996, Hopkins et al. 2001). Thus it is possible that our high- z $\text{H}\alpha$ sample would require a correction larger than 1 mag. The fact that high- z CFRS galaxies exhibit more irregular/starbursting morphologies (Brinchmann et al. 1998) may also argue for a larger correction. However comparison of our $\text{H}\alpha$ results with our 2800-Å data (Section 6.4) suggests that the average reddening correction cannot be much larger. This strengthens our 1 mag assumption for I -band selected CFRS sample. We note also that $\text{H}\alpha$ attenuations based on radio data are larger by 0.2 ± 0.2 mag on average than using Balmer decrements (see e.g. Bell & Kennicutt 2001, Caplan & Deharveng 1986). All of these uncertainties in reddening correction are small compared to the statistical uncertainty in our final luminosity density estimate.

5 SAMPLE PROPERTIES

5.1 Survey detection limits

The CFRS I -band selection implies that intrinsically bright galaxies, ($M^* \pm 1$), are targeted at high redshift, i.e. with $M(\text{B}_{\text{AB}}) \simeq -21 \pm 1$ mag at $z > 0.5$. This bias is shown in the top panel of Fig. 4, which displays both our low- and high- z $\text{H}\alpha$ samples. The ($z \leq 0.3$) and ($z > 0.5$) samples contain respectively ~ 10 and 100 per cent of galaxies brighter than $M(\text{B}_{\text{AB}}) = -20$ mag. The low panel of Fig. 4 shows the corresponding $\text{H}\alpha$ luminosities for the galaxies as a function of redshift. The detection limit of emission lines in the CFRS spectra is about 10 Å in terms of observed equivalent width. The dotted line represents a 10 Å lower limit in terms of line luminosity assuming the emission observed in the I -band ($\lambda_c = 8320$ Å) at the survey magnitude limit, $I_{\text{AB}} = 22.5$, i.e. a line flux equivalent to $10 \text{ Å} \times (1.5 \times 10^{-9})10^{-0.4 \times 22.5}$ in $\text{erg s}^{-1} \text{ cm}^{-2}$. This limit is correct for our low- z sample since at $z \simeq 0.26$ $\text{H}\alpha$ falls at the centre of the I -band. There is no observational selection to introduce an upper limit at large equivalent widths. For our high- z sample, we

preselected the galaxies to have observed $\text{EW}([\text{O II}]) \sim 10$ Å and this introduces an effective detection limit of observed $\text{EW}(\text{H}\alpha) \sim 22$ Å (see Table 2). The $\text{H}\alpha$ high- z detection limit is shown with $\text{EW} = 22$ Å assuming either a flat spectrum with $I_{\text{AB}} = J$, or a colour term ($I_{\text{AB}} - J$) $\simeq 1.5$. In the latter case, we see that $\text{H}\alpha$ can be detected below the ‘limit’ because of the spread in the observed $[\text{O II}]$ - $\text{H}\alpha$ relation, and also in the colour term. The rest-frame $\text{EW}(\text{H}\alpha)$ varies from 1 to 140 Å, with a median of 33 Å. This range is similar for instance to $\text{H}\alpha$ EW observed in the SAPM b_J -selected sample at $\langle z \rangle = 0.05$ (Tresse et al. 1999).

5.2 $\text{H}\alpha$ and B -band luminosities

Fig. 6 shows the relation between $L(\text{H}\alpha)$ and $M(\text{B}_{\text{AB}})$ of the CFRS galaxies at $z \leq 0.3$, and at $z > 0.5$. The high- z galaxies continue to follow the tight relation seen in the low- z sample, first noted by Tresse & Maddox (1998), $M(\text{B}_{\text{AB}}) = 46.7 - 1.6 \log L(\text{H}\alpha)$. The brighter in B_{AB} a galaxy is, the larger the $\text{H}\alpha$ luminosity. The scatter in this relation is much larger than the measurement uncertainties, and so reflects genuine differences between the different physical conditions within each galaxy, mainly the metallicity, the ionization parameter, the intrinsic dust and the recent star-formation history. The dotted line in the bottom panel of Fig. 6 corresponds to an observed 10-Å $\text{EW}(\text{H}\alpha)$ for galaxies with an Sab spectral energy distribution (SED) with $I_{\text{AB}} = 22.5$ and $0 < z < 1$. The precise location of the line depends on the assumed SED, but it corresponds approximately to the detection limit for the low- z sample. It is clear that the galaxy distribution is almost all above this line. As discussed in Section 5.1, we preselected the high- z galaxies on their $[\text{O II}]$ emission, so although there is not a sharp limit on $\text{EW}(\text{H}\alpha)$, we are more likely to observe galaxies with $\text{EW}(\text{H}\alpha) > 22$ Å. The dashed line in Fig. 6 shows the 22-Å $\text{EW}(\text{H}\alpha)$ limit. Although there is no observational constraint to exclude galaxies with high $L(\text{H}\alpha)$ at a given $M(\text{B}_{\text{AB}})$, there clearly is an upper limit to the observed $L(\text{H}\alpha)$ which increases with $M(\text{B}_{\text{AB}})$. The highest $L(\text{H}\alpha)$ for a given $M(\text{B}_{\text{AB}})$ corresponds to the galaxies with the strongest and most recent phases of star formation.

Fig. 7 explicitly shows the ratio $L(\text{H}\alpha)/L(\text{B}_{\text{AB}})$ as a function of $M(\text{B}_{\text{AB}})$. The $L(\text{H}\alpha)/L(\text{B}_{\text{AB}})$ ratio increases for brighter galaxies, reflecting the non-linear relation between $L(\text{H}\alpha)$ and $L(\text{B}_{\text{AB}})$ inferred from Fig. 6. Within the low- z sample, galaxies with $M(\text{B}_{\text{AB}}) < -20$ appear to have a slightly lower ratio, but after reddening correction, this is less apparent, probably because of the luminosity dependence of the reddening. Also, after reddening correction the data appear more scattered.

The high- z galaxies all have $M(\text{B}_{\text{AB}}) < -20$ and show a higher $L(\text{H}\alpha)/L(\text{B}_{\text{AB}})$ ratio than the equivalent low- z galaxies. This difference is mostly due to the higher EW limit of our high- z sample, as demonstrated by the dotted and dashed lines, which show the expected ratio for $\text{EW}(\text{H}\alpha) = 10$ Å and $\text{EW}(\text{H}\alpha) = 22$ Å galaxies respectively, as in Fig. 6. A small part of the difference is likely to be real evolution in the $L(\text{H}\alpha)/L(\text{B}_{\text{AB}})$ ratio. In Section 6.3 we find that the $\text{H}\alpha$ luminosity density increases as $(1+z)^{4.1}$, whereas Lilly et al. (1996) found that the B -band luminosity density increases as $(1+z)^{2.7}$, so we expect $\log(L(\text{H}\alpha)/L(\text{B}_{\text{AB}}))$ to increase by roughly 0.2 between the

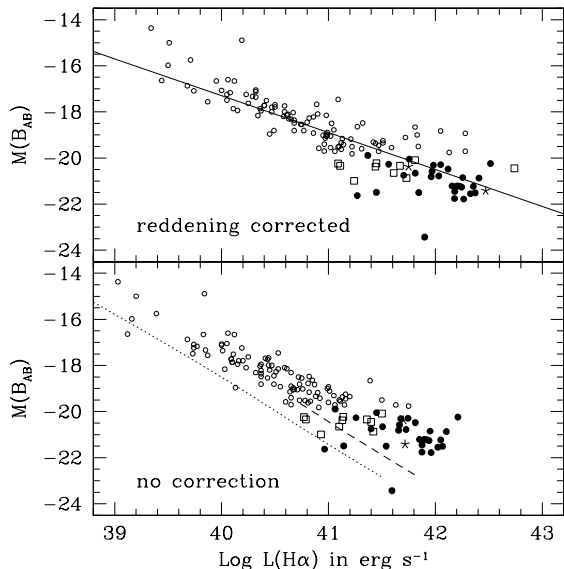


Figure 6. $\log L(H\alpha)$ versus $M(B_{AB})$ with reddening correction (top), with no correction (bottom). The different symbols are defined in Fig. 4. The solid line is $M(B_{AB}) = 46.7 - 1.6 \log L(H\alpha)$, as first noted by Tresse & Maddox (1998). The dotted and dashed lines correspond to an Sab galaxy with $0 < z < 1$, $I_{AB} = 22.5$, and observed $EW(H\alpha) = 10$ and 22 \AA respectively.

low- and high- z samples, even if the selection limits were the same.

Fig. 7 suggests that the upper limit observed in Fig. 6 in terms of $L(H\alpha)/L(B_{AB})$ is independent of B -band absolute magnitude. Since $H\alpha$ flux originates mainly from UV photoionizing photons ($< 912 \text{ \AA}$) it traces only massive, young, short-lived stars (OB stars, $t < \text{few} \times 10^6 \text{ yr}$), while the rest-frame B -band flux is dominated by longer-lived stars (type A). The highest ratio will be seen during a burst of star-formation, during which the ratio directly reflects the Initial Mass Function. Thus a constant upper limit is in agreement with the hypothesis of a universal Initial Mass Function (IMF): for a certain amount of massive OB stars formed, there is always the same amount of intermediate, type A, stars.

5.3 $H\alpha$ luminosities and colours

Fig. 8 shows $(V-I)_{AB}$ rest-frame colours of the low- and high- z galaxy samples. The most striking feature of the diagram is that the high- z galaxy sample has a much higher mean $L(H\alpha)$, as discussed in Section 5.2.

There is no significant correlation between $H\alpha$ luminosities and the rest-frame $(V-I)$ colours. This is consistent with the whole CFRS sample, which shows that no correlation between $M(B_{AB})$ and rest-frame $(U-V)$ colours (see Figure 5 in Lilly et al. 1995). This supports the idea that the $H\alpha$ flux depends on the instantaneous star formation rate and on the time since the last burst.

The median colours of the low- and high- z samples are the same within the uncertainties: 0.58 ± 0.15 at low- z and 0.53 ± 0.11 at high- z . In the low- z sample, there are a few strong $H\alpha$ emitters which have red colours. They show spec-

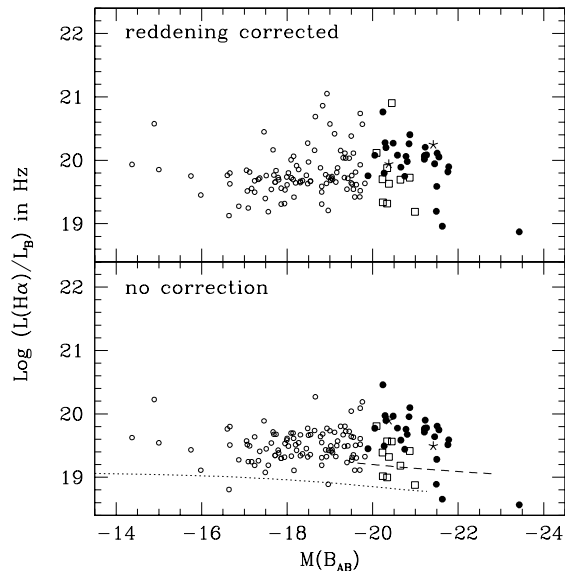


Figure 7. Logarithmic difference between $L(H\alpha)$ and $L(B_{AB})$ versus $M(B_{AB})$ with reddening correction (top), with no correction (bottom). The different symbols are defined in Fig. 4. The dotted and dashed lines are the same as in Fig. 6.

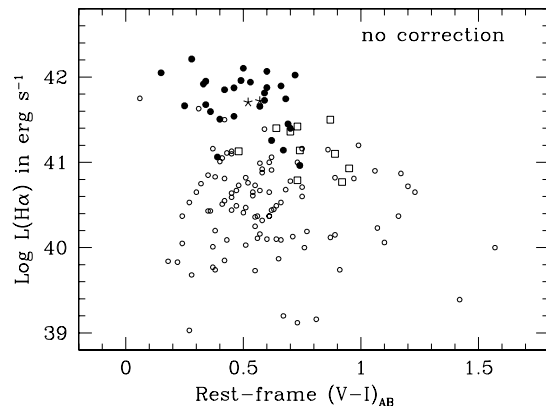


Figure 8. $\log L(H\alpha)$ versus rest-frame $(V-I)_{AB}$. The different symbols are defined in Fig. 4.

tral features (Ca H and K, G band, MgI) indicating the presence of a dominant old population (see Tresse et al. 1996). In the high- z sample we do not see $H\alpha$ in galaxies redder than rest-frame $(V-I) = 0.8$. This could simply be due to the lower sampling rate in the observed high- z sample, but also the higher EW detection limit for the high- z sample (see Section 5.1) biases against detecting galaxies with a red continuum and a weak $H\alpha$ flux.

5.4 $[O II]-H\alpha$ luminosity ratio

In other surveys where $H\alpha$ could not be observed, the $[O II]$ line has frequently been used to provide SFR estimates by making the assumption that the $[O II]-H\alpha$ ratio is constant and equal to that derived from local samples. These two lines

Table 2. Medians and *rms* dispersions of the [O II]–H α luminosity ratio.

Sample	N	$\langle z \rangle$	Median	<i>rms</i> (%)
No correction				
$0 < z < 0.1$, SAPM	859	0.05	0.55	60
$0 < z \leq 0.3$, CFRS [†]	40	0.24	0.97	164
$0.5 < z < 1.1$, CFRS [‡]	30	0.73	0.46	68
Reddening corrected				
$0 < z \leq 0.3$, CFRS [†]	40	0.24	1.78	184
$0.5 < z < 1.1$, CFRS [‡]	30	0.73	0.84	71

[†]The $0 < z \leq 0.3$ sample has been restricted to galaxies with $M(B_{AB}) \geq -20$.

[‡]The $0.5 < z < 1.1$ sample contains only galaxies with $M(B_{AB}) < -20$.

are closely related since they both come from star formation activity in H II regions. However, [O II] depends also on the metal fraction present in the gas, and on the ionization parameter, which means that the observed scatter about the mean relation is large. For instance in the SAPM sample (Tresse et al. 1999) and the Kennicutt (1992) data, the scatter in the EW ratio is as large as 60 per cent. Variations in the continuum colour may increase the scatter in the EW measurements compared to line luminosities, but the scatter is very large even in the luminosity ratio. Fig. 9 shows the correlation between [O II] and H α luminosities for our CFRS data. The medians and *rms* dispersions are listed in Table 2. The high-*z* sample tends to have a lower [O II]–H α ratio than the overall mean. Though it is tempting to suggest that this is an evolutionary effect, we argue that it is in fact evidence for a luminosity dependence in the [O II]–H α ratio.

Fig. 10 shows the ratio of [O II]/H α fluxes as a function of $M(B_{AB})$, and we see that there is a systematic decrease towards brighter galaxies. Most of the brighter galaxies are from the high-*z* sample, but there are a small number of bright galaxies at low redshift (shown as open squares) which also follow the trend. This argues against an evolutionary effect. A similar luminosity dependence in the [O II]/H α ratio has been previously noted in nearby surveys, in particular in the Nearby Field Galaxy Survey (NGFS; Jansen, Franx & Fabricant 2001), in the 15R survey (Carter et al. 2001), and in the SAPM (Charlot et al. 2002). Since these surveys are both restricted to very low redshifts we can exclude that the effect is due to evolution. The correlation between [O II]/H α and $M(B_{AB})$, and the scatter in the ratio is related to changes in the effective gas parameters (ionization, metallicity, dust content) as a function of luminosity, rather than systematic changes in SFR per unit $M(B_{AB})$ (see e.g. Jansen et al. 2001, Charlot et al. 2002). This systematic change in ratio means that SFR estimates based on [O II] line measurements may be significantly biased if the local average ratio of [O II]/H α is assumed. This effect will be particularly important at higher redshifts where current samples tend to be restricted to galaxies that are more luminous than the average in local samples. For instance, within the CFRS this ratio varies by a factor 2 from the low- to high-*z* samples. Note that when we correct for reddening we have assumed a constant A_V for our high-*z* sample. If A_V is luminosity dependant as discussed in Section 4, this constant

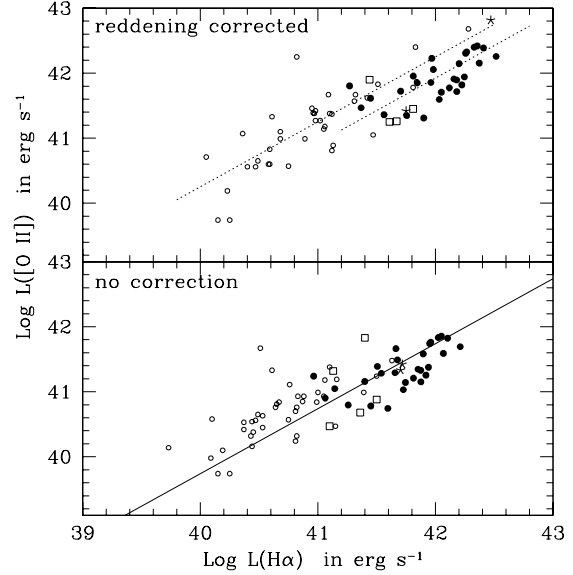


Figure 9. Log L([O II]) versus log L(H α) with reddening correction applied to both emission lines (top), with no correction (bottom). The dotted lines are the medians of the low- and high-*z* ratios, and the plain line is the local ratio (see Table 3.2). The different symbols are defined in Fig. 4.

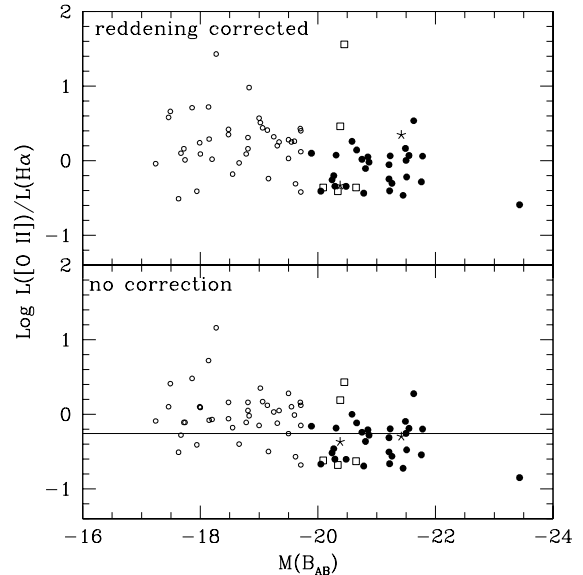


Figure 10. Logarithmic difference between [O II] and H α luminosity versus $M(B_{AB})$ with reddening correction applied to both emission lines (top), with no correction (bottom). The plain line is the local ratio (see Table 3.2). The different symbols are defined in Fig. 4.

correction will not remove the correlation shown in Fig. 9, upper panel. We find no correlation between [O II]/H α and rest-frame (V–I) colour (Fig. 11).

6 H α LUMINOSITY AND SFR DENSITIES

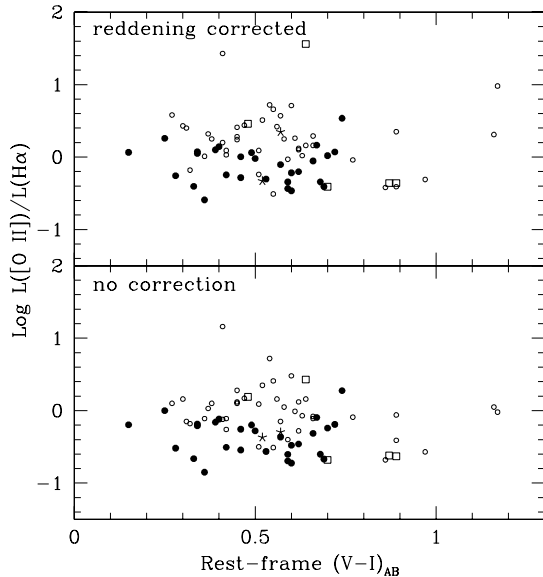


Figure 11. Logarithmic difference between [O II] and $H\alpha$ luminosity versus $(V-I)_{AB}$ with reddening correction applied to both emission lines (top), with no correction (bottom). The different symbols are defined in Fig. 4.

6.1 Completeness correction

In the following completeness correction, we account for the selection of our high- z $H\alpha$ (see Section 2) from the CFRS survey.

For the original CFRS sample, objects were selected as spectroscopic targets solely on the basis of their I -band photometry, $17.5 \leq I_{AB} \leq 22.5$, with no star/galaxy classification (see Le Fèvre et al. 1995). Our low- z sample includes all CFRS targets in the relevant redshift range, and so the $H\alpha$ luminosity function can be estimated using the standard V_{max} technique, as described by Tresse & Maddox (1998). For our high- z sample, the targets were subject to a second selection based on their [O II] emission, and so estimating the $H\alpha$ luminosity function requires a slight modification to the V_{max} technique.

For each galaxy we estimate the observable volume by calculating the volume between the maximum and minimum redshift at which it could have been in the sample given the apparent magnitude and redshift limits and the solid angle of the CFRS. Not all galaxies in the CFRS photometric sample were targeted for spectroscopy in the CFRS, thus we have effectively observed only a fraction of the total observable galaxies in three CFRS fields, $f_{spec} = N(CFRS|spec)/N(CFRS|phot) = 3 \times 434/2452$, where $N(CFRS|spec)$ is the total number of galaxies with measured redshifts in the three observed CFRS fields, and $N(CFRS|phot)$ is the corresponding number of galaxies detected in the photometric sample.

Since we have also selected galaxies away from OH sky lines, we must allow for the consequent gaps in redshift where we have excluded galaxies. For each galaxy we calculate the observable volume using $(V_{max} - V_{min})$, and renormalize the resulting number density by the ratio of the number of galaxies away from OH lines

to the total number CFRS galaxies within the allowed redshift range. This corresponds to a fraction $f_{OH} = N(OH)/N(CFRS|(spec \ \& \ 0.50 < z < 1.05)) = 84/157$, where $N(OH)$ is the number of CFRS galaxies with measured redshifts away from OH lines, and $N(CFRS|(spec \ \& \ 0.50 < z < 1.05))$ is the total number of CFRS galaxies with measured redshifts in our selected range.

We must make a further correction because we selected our target galaxies to have observed $EW([O \ II]) > 12 \text{ \AA}$. This introduces a bias to higher $H\alpha$ fluxes, as can be seen from Fig. 9. We used the observed median [O II]/ $H\alpha$ ratio (see Table 2) to estimate the average line flux limit introduced by the preselection. Since the scatter about the mean relation is large ($\sim 50\%$), the [O II] limit does not introduce a sharp cut in $H\alpha$, but a smooth drop in completeness. Assuming that the scatter is approximately Gaussian, the incompleteness will be proportional to the corresponding error function. Thus, when calculating the observable volume for each galaxy, we weighted the volume integral according to $\frac{1}{2}(\text{erf}((z - z_{lim})/\sigma) + 1)$, where z_{lim} is the maximum redshift that the median [O II]- $H\alpha$ relation would have introduced, and ($\sigma = 0.2$) is determined by the scatter in the relation.

This procedure corrects for the incompleteness near the observed $L(H\alpha)$ limit, but does not account for the fact that we have observed only a fraction of the available galaxies. We calculated this correction factor assuming one of two extreme cases: either that the high $EW([O \ II])$ galaxies are representative of the complete sample; or that they contribute all of the $H\alpha$ flux (equivalent to assuming that $H\alpha$ is never seen in emission without [O II]). In the first case there are two correction factors: the fraction of galaxies with $EW([O \ II]) > 12 \text{ \AA}$, $f_{[OII]} = 63/84$; and the fraction that we observed with ISAAC, $f_{obs} = 33/63$. The overall correction factor from observed luminosity to estimated total luminosity is then $f_{rep} = f_{obs} f_{[OII]} f_{OH} f_{spec} = 0.1116$. In the second case, we make the assumption that all of the $H\alpha$ luminosity would be seen in the [O II] selected sample, which is equivalent to setting the factor $f_{[OII]} = 1$. This leads to an overall correction factor $f_{all} = f_{obs} f_{OH} f_{spec} = 0.1488$. The ratio between these two extremes is $f_{rep}/f_{all} = 0.75$, and so a robust limit on this source of uncertainty is 0.125 in $\log(\phi)$.

An intermediate estimate of the correction factor can be obtained from the SAPM survey (Tresse et al. 1999) which has [O II] and $H\alpha$ measurements for all galaxies in a local sample. If we split the SAPM into galaxies with observed $EW([O \ II]) > 12 \text{ \AA}$, and galaxies with observed $EW([O \ II]) \leq 12 \text{ \AA}$, including non [O II] emitters, we find that the mean $H\alpha$ luminosity for high-[O II] galaxies is about four times that for low-[O II] galaxies. In the complete high- z CFRS sample, we have 251 galaxies with $EW([O \ II]) > 12 \text{ \AA}$, and 72 galaxies $EW([O \ II]) \leq 12 \text{ \AA}$. Ignoring possible evolutionary effects and complications due to weighting by different accessible volumes, the ratio of mean $H\alpha$ luminosities for our high- z $EW([O \ II])$ samples will be the same. Thus the total $H\alpha$ luminosity would be 1.07 times our estimated total $H\alpha$ luminosity using the correction factor f_{rep} , which translates into 0.03 in $\log H\alpha$ luminosity density. This is much less than the one sigma statistical uncertainty derived in the next sections, and so for our best luminosity function estimate we use f_{rep} .

6.2 The H α luminosity function

The resulting luminosity function (LF) and its Schechter (1976) fit are shown in Fig. 12. The best fit values are:

$$\begin{aligned}\alpha &= -1.31 \pm 0.11, \\ \phi^* &= 10^{-2.39 \pm 0.06} \text{ Mpc}^{-3}, \\ L^* &= 10^{42.37 \pm 0.06} \text{ ergs}^{-1}.\end{aligned}$$

The uncertainties on these parameters are correlated as can be seen from the χ^2 contours shown in Fig. 13. The evolution of the H α LF from $z \sim 0$ to $z \sim 1$ is now clearly demonstrated. The Gallego et al. (1995) H α LF at $z \simeq 0$ is a factor ~ 2 lower than Tresse & Maddox (1998) H α LF at $\langle z \rangle = 0.2$, which is in turn a factor ~ 5 lower than our present data at $\langle z \rangle = 0.7$. The strong evolution appears closely related to the (ϕ^* , L^*) parameters rather than to the faint-end slope, α .

The LF from our non reddening corrected H α flux data is presented in Fig. 14 where our previous best LF fit is shifted by a factor 2.02 in log towards fainter luminosities (2.02 corresponds to $A_V = 1$ mag, see Section 4). The uncorrected LFs from Yan et al. (1999) and Hopkins, Connolly & Szalay (2000) are also shown. The data of Yan et al. are composed of 33 H α +[N II] blends detected at $0.75 < z < 1.9$ with a similar range of EW as our sample, from a few Å to ~ 130 Å. We note that their LF extends to brighter H α luminosities than ours; this is certainly due to the fact that their galaxies have brighter H α on average, but also due to their average [N II] λ 6583/H α correction of 0.3. In the local SAPM data from Tresse et al. (1999), this ratio varies from 0.7 to 0.1 for a similar EW range, which implies that the correction to H α +[N II] fluxes varies from 48% to 12%. Hopkins et al. (2000) combined their data with those of Yan et al. (1999), and find a similar LF to Yan et al. We also plotted the preliminary narrow-band non reddening corrected H α LFs from Jones & Bland-Hawthorn (2001) at $z = 0.08$, $z = 0.24$ and $z = 0.40$. Since they do not fit their data with a Schechter function, we simply joined their data points in Fig. 14. To compare to their data we plotted our ($0 < z \leq 0.3$) H α LF shifted by a factor 2.02 in log towards fainter luminosities. Their LFs are broadly consistent with our low- z LF. Their data at $z = 0.24$ and $z = 0.40$ show an evolution in H α luminosities. Overall the strong evolution of the H α LF is clearly demonstrated from $z \sim 0$ to $z \sim 1.3$.

In Figs. 12&14, the different shape of the LFs is likely to be due to different sample selection. In particular the LF for the UV -selected local sample of Sullivan et al. (2000) has a shape quite different compared to the H α -selected LF of Gallego et al. (1995), or with ours at low- z (roughly corresponding to a rest-frame R selection) and at high- z (roughly corresponding to a rest-frame B selection). A similar difference in shape has already been noted in comparisons of broad-band LFs from B -selected samples such as the Autofib Redshift Survey (Ellis et al. 1996) to LFs from I - or R -selected samples such as the CFRS (Lilly et al. 1995) and the CNOC2 (Lin et al. 1999). Samples which select galaxies on their UV continuum are more dominated by blue, late-type galaxies, which steepen the slope α , and brighten L^* , because of k -correction effects. The LF shape derived from samples with narrow-band emission-line selection (Gallego et al. 1995), or with rest- B continuum selection (this paper) are similar. This is not surprising if we account for the close

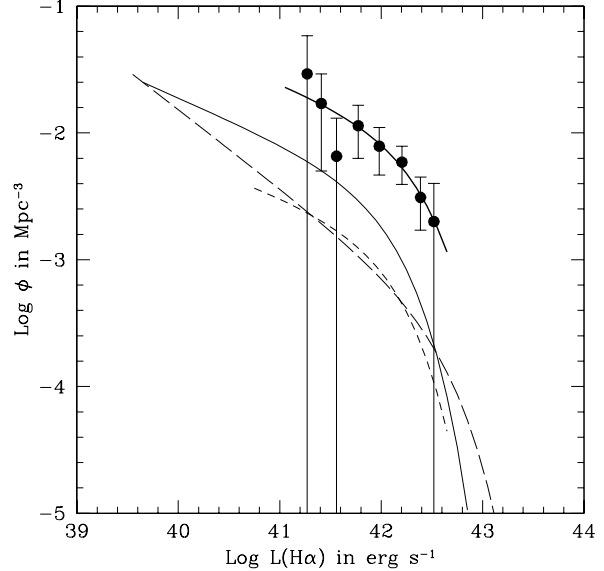


Figure 12. The reddening corrected H α luminosity function for four galaxy samples at different redshifts. The filled circles are our data measurements at $0.5 < z < 1.1$, and the thick solid curve is the best Schechter fit to our data. The density error bars assume Poisson statistics. The thin solid curve is the Tresse & Maddox (1998) H α LF at $\langle z \rangle = 0.2$ ($\alpha = -1.35 \pm 0.06$, $\phi^* = 10^{-2.83 \pm 0.09} \text{ Mpc}^{-3}$, $L^* = 10^{42.13 \pm 0.13} \text{ erg s}^{-1}$). The short-dashed curve is the Gallego et al. (1995) H α LF at $z \simeq 0$ from an emission line-selected sample based on slitless spectra ($\alpha = -1.3 \pm 0.2$, $\phi^* = 10^{-3.2 \pm 0.2} \text{ Mpc}^{-3}$, $L^* = 10^{42.15 \pm 0.08} \text{ erg s}^{-1}$). The long-dashed curve is the Sullivan et al. (2000) H α LF at $\langle z \rangle = 0.15$ from a UV -selected sample ($\alpha = -1.62 \pm 0.10$, $\phi^* = 10^{-3.82 \pm 0.20} \text{ Mpc}^{-3}$, $L^* = 10^{42.65 \pm 0.14} \text{ erg s}^{-1}$).

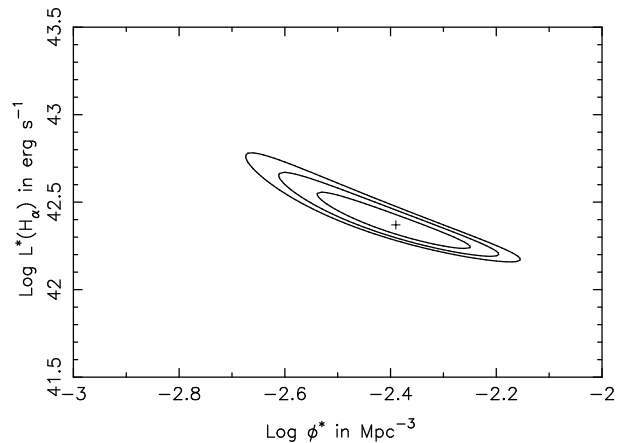


Figure 13. Contours of χ^2 for Schechter function fit plotted in Fig. 12. The contours correspond to 1σ intervals in the parameters ϕ^* and L^* with $\alpha = -1.31$.

relation between B magnitudes and H α luminosities (see Fig. 4). Since we observe that H α is tightly correlated to absolute B magnitude, we expect H α LFs to be about same shape as the $M(B_{AB})$ LF of mid- and late-type galaxies.

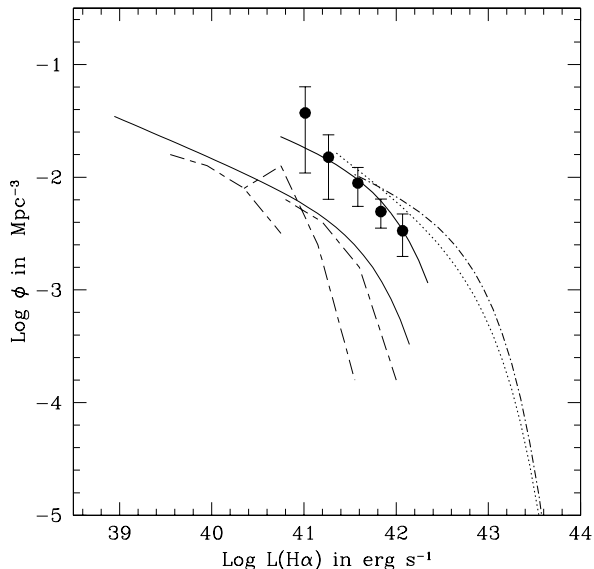


Figure 14. The H α luminosity function with no reddening correction applied for five galaxy samples at different redshifts. The filled circles are our data measurements not corrected for reddening at $0.5 < z < 1.1$, and the solid curve is the best fit to our reddening corrected data plotted in Fig. 12 but shifted in X-axis by $-\log 2.02$. The thin solid curve is the Tresse & Maddox (1998) H α LF but shifted in X-axis by $-\log 2.02$, at $0 < z \leq 0.3$. The short-long dashed curves are the preliminary H α LF from Jones & Bland-Hawthorn (2001) from left to right respectively at $z = 0.08$, $z = 0.24$, $z = 0.40$. The dot-dashed curve is the Yan et al. (1999) H α LF at $0.7 < z < 1.9$ with $\phi^* = 10^{-2.77} \text{ Mpc}^{-3}$, $L^* = 10^{42.85} \text{ erg s}^{-1}$, and α assumed equal to -1.35 , and the dotted curve is the Hopkins et al. (2000) H α LF at $0.7 < z < 1.8$ which includes the data of Yan et al. (1999).

6.3 H α luminosity densities

A minimal estimate of the luminosity density can be obtained by simply summing up $L(\text{H}\alpha)/V_{\text{max}}$ for each galaxy, weighted by f_{rep} (see Section 6.1). This gives the directly observed luminosity density; $\mathcal{L}(\text{H}\alpha) = 10^{40.04} \text{ erg s}^{-1} \text{ Mpc}^{-3}$ at $0.5 < z < 1.1$. For a Schechter function, the luminosity density is dominated by $\sim L^*$ galaxies, so galaxies outside the observed luminosity range will not introduce large errors so long as galaxies near L^* are included, and the faint-end slope α is not as steep as -2 . Indeed the estimate from analytically integrating our best Schechter function gives $\mathcal{L}(\text{H}\alpha) = 10^{40.10 \pm 0.05} \text{ erg s}^{-1} \text{ Mpc}^{-3}$ at $\langle z \rangle \simeq 0.7$. If we account for the uncertainty in $\log(\phi)$ as described in Section 6.1, we obtain $10^{40.22 \pm 0.05} \text{ erg s}^{-1} \text{ Mpc}^{-3}$. For the low- z sample of Tresse & Maddox (1998), using the sum of the individual densities or the LF integration, we find the same total H α luminosity density, respectively $10^{39.45}$ and $10^{39.44 \pm 0.04} \text{ erg s}^{-1} \text{ Mpc}^{-3}$. The luminosity density contributed by galaxies outside the observed range is very small, so the correction factor to extrapolate to all luminosities is very close to unity. In addition to our high- z estimate, we divided the high- z sample at the median redshift, $z = 0.702$, into two bins. Using the sum of the individual densities in each bin, we find $10^{40.05 \pm 0.05} \text{ erg s}^{-1} \text{ Mpc}^{-3}$ at $\langle z \rangle = 0.6$ and $10^{40.21 \pm 0.17} \text{ erg s}^{-1} \text{ Mpc}^{-3}$ at $\langle z \rangle = 0.8$. We estimated

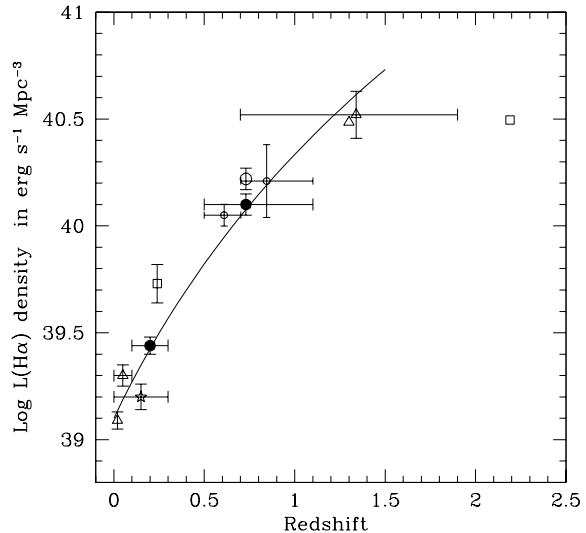


Figure 15. The evolution of H α luminosity density with redshift with reddening-corrected H α data summarized in Table 3. The curve represents an evolution proportional to $(1+z)^{4.1}$. The filled circles represent our CFRS broad-band I -selected data at $\langle z \rangle = 0.3$ and 0.7 , and the large open circle corresponds to our high- z data but using the correction factor f_{all} (see Section 6.1). The two small open circles represent our high- z sample divided into two bins at $\langle z \rangle = 0.6$ and $\langle z \rangle = 0.8$. The other points in the diagram are as follows. Triangles represent slitless spectroscopic surveys: (UCM) Gallego et al. (1995) at $z \sim 0$; (KISS) Gronwall et al. (1999) at $z = 0.05$; Hopkins, et al. (2000) at $z = 1.3$ and Yan et al. (1999) at $z = 1.34$. Squares represent narrow-band filter surveys: Pascual et al. (2001) at $z = 0.24$; Moorwood et al. (2000) at $z = 2.2$. The star represents the FOCA broad-band UV -selected data of Sullivan et al. (2000) at $\langle z \rangle = 0.15$.

the uncertainties by slightly varying the redshift cut about the median redshift and measuring the *rms* dispersion. Even though the small number of galaxies (15) in each bin makes the statistics poorer than using the entire high- z sample, there is a suggestion of an increase in the luminosity density over the redshift range $0.5 < z < 1.1$.

In Fig. 15, we present reddening corrected H α luminosity densities derived from H α LFs as a function of redshift (see also Table 3). The increase of the H α luminosity density is proportional to $(1+z)^{4.1 \pm 0.3}$ from $z \sim 0$ to 1.3 . We note that the UV -selected data from Sullivan et al. (2000) at $z \sim 0.15$ is slightly below this evolution. This is because their LF has a brighter L^* (due to two extremely bright H α luminosities), and has a lower ϕ^* . Their α is also steep, but this does not contribute much to the overall luminosity density. See also Section 6.2.

Regarding possible narrow-line AGN contamination, we do not exclude Seyfert 2 or LINER spectra in either our low- or high- z data. This allows direct comparison with SFRs derived from continuum luminosity densities where no such exclusion is done. Also it avoids possible confusions from the fact that different criteria may be used to identify active galaxies in different samples. At $z \lesssim 0.3$, the fraction of AGN-like spectra can vary from few per cent to 40 per cent depending on the selection criteria. For example, it is 8–17

Table 3. H α luminosity densities estimated from the H α luminosity function.

Redshift range	N	$\langle z \rangle$	Log $\mathcal{L}(\text{H}\alpha)^\dagger$	Selection ‡	Reference
$z \leq 0.045$	176	0.02	39.09 \pm 0.04	SLS H α -selected, UCM	Gallego et al. (1995)
$0 < z < 0.1$	1100	0.05	39.30 \pm 0.05	SLS H α -selected, KISS	Gronwall et al. (1999)
$0 < z < 0.4$	88	0.15	39.20 \pm 0.06	UV-selected, FOCA	Sullivan et al. (2000)
$0 < z \leq 0.3$	138	0.21	39.44 \pm 0.04	I-selected, CFRS	Tresse & Maddox (1998)
$0.228 < z < 0.255$	37	0.24	39.73 \pm 0.09	NBF H α -selected	Pascual et al. (2001)
$0.5 < z < 1.1$	33	0.73	40.10 \pm 0.05	I-selected, CFRS	This paper
$0.7 < z < 1.8$	17/37	1.3	40.18+log(2.02) ^{1,2}	SLS H α -selected	Hopkins et al. (2000)
$0.7 < z < 1.9$	33	1.34	40.21+log(2.02) ¹	SLS H α -selected	Yan et al. (1999)
$2.175 < z < 2.225$	6	2.19	40.19+log(2.02) ^{1,2}	NBF H α -selected	Moorwood et al. (2000)

$^\dagger \mathcal{L}(\text{H}\alpha)$ in units of $\text{erg s}^{-1} \text{Mpc}^{-3}$.

‡ The H α -selected surveys use either narrow-band filters (NBF) or slitless spectroscopy (SLS). These samples can be contaminated by other emission-line features if the lines are not fully spectroscopically confirmed, in particular at high redshifts.

¹Assuming the canonical $A_V=1$ mag extinction.

²Based on the Yan et al. (1999) H α luminosity function.

per cent in the CFRS low- z sample (Tresse et al. 1996); 8 per cent in the local UCM (Gallego et al. 1995); 17–28 per cent in the 15R survey (Carter et al. 2001). Detailed studies as for instance done by Ho, Filipenko & Sargent (1997) find a fraction of 43 per cent in their blue-selected survey. UV-selected samples contain almost no narrow-line AGN (Contini et al. 2002), this agrees with the common picture that active galaxies are more dusty than normal galaxies. If an active nucleus is present in the central region of a galaxy, then the H α flux is not correlated directly to forming stars, but is a mixture from both the AGN and SFR. This makes it difficult to separate the stellar from the AGN contribution in the total luminosity density from optically-selected galaxy surveys. The SFR density diagrams derived from such surveys must depend on the fraction of AGN-like galaxies, and on any global cosmic evolution in the nuclear activity of galaxies. In the UCM, the 8 per cent of AGN-like galaxies contribute to 15 per cent to the overall luminosity density (Pascual et al. 2001). If this fraction stays about constant up to ~ 1 , then the H α -derived SFRs are contaminated by no more than 15 per cent AGN light. This is an upper limit to the contamination, because excluding AGN-like galaxies will exclude the light from present star formation as well as their AGN contribution.

6.4 Star-formation rate densities

In Fig. 16 we plot SFR densities based on several recent reddening-corrected H α measurements. We use the Kennicutt (1998, hereafter K98) transformation between H α luminosity (units erg s^{-1}) and SFR (units $M_\odot \text{yr}^{-1}$) for solar abundances and a Salpeter IMF including stars in the 0.1–100 M_\odot mass range: $\log L(\text{H}\alpha) = 41.10 + \log \rho_*$. For comparison, we also plot the 2800-Å CFRS data from which Lilly et al. (1996) derived a growth proportional to $(1+z)^{3.9\pm 0.75}$. We use the K98 transformation, $\log L_{UV}(\text{erg s}^{-1} \text{Hz}^{-1}) = 27.85 + \log \rho_*(M_\odot \text{yr}^{-1})$ which includes no dust correction. As shown in the figure, our H α SFR density growth, $(1+z)^{4.1\pm 0.3}$ is entirely consistent with the UV SFR density growth. To make compatible both the H α and UV SFR densities, a shift in SFR density of a factor of 3.20 is necessary. This ratio corresponds to the dust

correction to the near UV data, and implies $A_V \simeq 1$ mag for a simple dust-screen model (Pei 1992). This is in agreement with the $L(2800\text{\AA})/L(\text{H}\alpha)$ ratio of $3.1\pm 0.4 \cdot 10^{-14} \text{Hz}^{-1}$ found by Glazebrook et al. (1999) with six CFRS H α data at $z \sim 0.9$. We note that a correlation of the H α /FUV ratio as a function of intrinsic luminosity has been found by e.g. Bell & Kennicutt (2001), Sullivan et al. (2001), Buat et al. (1999). This will affect little our result since the low-luminosity galaxies contribute little to the total density, and since the FUV ($\leq 2000 \text{\AA}$) is more sensitive to dust attenuation (~ 1.4 mag) than the near UV at 2800 Å (~ 1 mag). In conclusion, our H α and 2800-Å SFR densities are broadly consistent assuming an attenuation of $A_V = 1$ mag.

Charlot et al. (2002) have derived SFRs of the local SAPM galaxies, using H α , [O II], [S II] and [N II]. They conclude that the true SFRs are typically two or three times higher than those derived from H α alone, using the K98 transformation, even after applying the usual mean reddening correction of $A_V = 1$ mag. The Charlot & Longhetti (2001) model accounts for the absorption of ionizing photons by dust in H II regions and the contamination of H α emission by stellar absorption. Including these effects they find that SFR estimators derived from H α , [O II], UV, and far-IR fluxes give consistent results. This would imply that the CFRS-UV SFR densities should be increased by a factor 5 or 6.

Our H α luminosity density estimates confirm the steep rise in SFR density for $0.1 < z < 1.1$, as found by Lilly et al. (1996). Since our results are based on independent H α measurements, the steep rise is unlikely to be due to extrapolation of the CFRS data to the 2800-Å luminosities as suggested by Cowie et al. (1999). Our measurements are inconsistent with the shallow rise of the 2500-Å luminosity density, $\propto (1+z)^{1.5}$, found by Cowie et al. (1999), and also the Sullivan et al. (2000) suggestion that the 2000-Å luminosity density is $\propto (1+z)^{1.7}$. At $z \sim 0.2$ the Sullivan et al. (2000) luminosity density is consistent with both our H α estimate and the Lilly et al. (1996) estimate, so the suggestion of a shallow slope is mainly driven by the low luminosity density at $z \sim 0.5 - 1$ found in the Cowie et al. (1999) survey. This survey covers a very small area ($\sim 30 \text{arcmin}^2$) compared to the CFRS ($\sim 500 \text{arcmin}^2$), and so

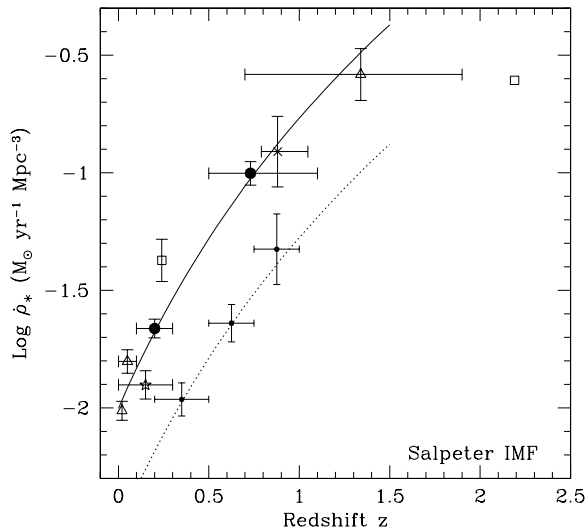


Figure 16. SFR densities based on reddening-corrected H α measurements. We have applied a correction of $A_V = 1$ mag for data which were not reddening corrected (see Table 3). SFR are derived from the K98 transformation, $\log L(\text{H}\alpha)(\text{erg s}^{-1}) = 41.10 + \log \rho_*(M_\odot \text{ yr}^{-1})$. Note that according to the Charlot & Longhetti (2001) model, the K98 H α transformation gives a SFR typically two or three times too low, even after reddening correction (see Section 6.2). The different symbols are defined in Fig. 15 with in addition the cross which shows the H α data on 6 CFRS galaxies at $\langle z \rangle = 0.9$ from which the SFR density has been derived using the broad-band CFRS luminosity function, and $L(2800 \text{ \AA})/L(\text{H}\alpha) = 3.1 \cdot 10^{-14} \text{ Hz}^{-1}$ (Glazebrook et al. 1999). The solid curve shows the $(1+z)^{4.1}$ evolution as shown in Fig. 15. For reference, we also show the 2800- \AA CFRS points from Lilly et al. (1996) using the K98 transformation $\log L_{UV}(\text{erg s}^{-1} \text{ Hz}^{-1}) = 27.85 + \log \rho_*(M_\odot \text{ yr}^{-1})$ which includes no dust correction. The dotted curve is the same as the plain curve shifted by a factor 3.2.

must be subject to much larger uncertainties due to cosmic variance. Thus we believe that the steeper rise in SFR is more likely to be correct.

The exact slope of the rise also depends on which local value is taken. For instance, using the H α SAPM data at $\langle z \rangle = 0.05$ Singleton (2001) found a lower value than Gallego et al. (1995), while Gronwall et al. (1998) finds a higher value using the H α KISS survey. Soon, the 2dFGRS and the SDSS should provide a more definitive local value. Whatever the local value, within our single survey the H α data demonstrate a rise in the SFR density by a factor of ~ 5 from $z \sim 0.2$ to $z \sim 0.7$. Our data and the Yan et al. data (1999), require strong evolution in the SFR density, which increases by a factor 12 from $z \sim 0.2$ to $z \sim 1.3$.

7 CONCLUSION

We have measured H α in emission for 30 galaxies from the CFRS at $0.5 < z < 1.1$ using the ISAAC ESO-VLT spectrograph. These data combined with those at $z \leq 0.3$ (Tresse & Maddox 1998) enabled us to derive measurements within a

single survey with well-controlled selection criteria, and with secure redshift measurements. Our results are the following:

(i) H α and B -band luminosities are tightly correlated at high- z as seen at low- z by Tresse & Maddox (1998). This strengthens the hypothesis of an universal IMF.

(ii) We demonstrate that the [O II]/H α ratio is luminosity dependent. Bright galaxies have ratios larger by a factor 2 than faint galaxies. This effect has already been observed in the local SAPM data (Charlot et al. 2002), in the 15R survey (Carter et al. 2001), and in the NFGS (Jansen et al. 2001).

(iii) Our best fit H α luminosity function at $\langle z \rangle = 0.7$ is $\alpha = -1.31 \pm 0.11$, $\phi^* = 10^{-2.39 \pm 0.06} \text{ Mpc}^{-3}$, $L^* = 10^{42.37 \pm 0.06} \text{ erg s}^{-1}$. Its shape is similar to the H α -selected luminosity function at $z \sim 0$ of Gallego et al. (1995), and also to the luminosity function at $\langle z \rangle = 0.2$ of Tresse & Maddox (1998). The strong evolution of the H α LF appears closely related to the (ϕ^*, L^*) parameters rather than to the faint-end slope α from $z \sim 0$ to $z \sim 1.3$.

(iv) We find an average $\text{SFR}(2800\text{\AA})/\text{SFR}(\text{H}\alpha)$ ratio of 3.2 using the K98 SFR transformations. Since the UV data are not dust corrected, this corresponds to $A_V \sim 1$ mag assuming a simple dust-screen model from Pei (1992). Accounting for Charlot et al. (2002) results of H α SFRs being larger by a factor of ~ 3 , it would imply that the UV CFRS densities need to be corrected by a factor of ~ 6 .

(v) The growth of the H α luminosity density is proportional to $(1+z)^{4.1 \pm 0.3}$ from $z \sim 0$ to $z \sim 1.3$. From independent data, we confirm the steep rise of the comoving SFR density as found by the CFRS 2800- \AA continuum data. The SFR density derived from H α luminosities increases by a factor 12 between $z \sim 0.2$ and $z \sim 1.3$.

In the near future, the VIRMOS-VLT Deep Survey (VVDS, Le Fèvre et al. 2001) will provide an wealth of data for measuring the star-formation rate density from $z \sim 0$ to $z \sim 5$ within a single galaxy survey.

ACKNOWLEDGMENTS

We thank the ESO staff at Garching and Paranal for their help in the acquisition of the data. We thank the referee for useful suggestions.

REFERENCES

- Bell E. F., Kennicutt R. C., 2001, ApJ, 548, 681
- Brinchmann J. et al., 1998, ApJ, 499, 112
- Buat V., Donas J., Milliard B., Xu C., 1999, A&A, 352, 371
- Caplan J., Deharveng L., 1986, A&A, 155, 297
- Carter B. J., Fabricant D. G., Geller M. J., Kurtz M. J., McLean B., 2001, 559, 606
- Charlot S., Longhetti M., 2001, MNRAS, 323, 887
- Charlot S., Kauffmann G., Longhetti M., Tresse L., White S. D. M., Maddox S. J., Fall S. M., 2002, MNRAS, in press (astro-ph/0111289)
- Contini T., Treyer M. A., Sullivan M., Ellis R. S., 2002, MNRAS, 330, 75
- Cowie L. L., Songaila A., Barger A. J., 1999, AJ, 118, 603
- Cuby J. G., Lidman C., Moutou C., Petr M., 2000, SPIE, 4008, 1036

- Ellis R. S., Colless M., Broadhurst T., Heyl J., Glazebrook K., 1996, MNRAS, 280, 235
- Gallego J., Zamorano J., Aragon-Salamanca A., Rego M., 1995, ApJ, 455, 1L
- Glazebrook K., Blake C., Economou F., Lilly S., Colless M., 1999, MNRAS 306, 843
- Gronwall C., 1999, in Proceedings of the Conference “After the Dark Ages: When Galaxies were Young”, ed. S. Holt, E. Smith, AIP, p. 335
- Hammer F., Gruel N., Thuan T. X., Flores H., Infante L., 2000, ApJ, 550, 570
- Ho L. C., Filippenko A. V., Sargent W. L. W., 1997, ApJ, 487, 568
- Hopkins A. M., Connolly A. J., Szalay A. S., 2000, AJ, 120, 2843
- Hopkins A. M., Connolly A. J., Haarsma D. B., Cram L. E., 2001, ApJ, 122, 288
- Jansen R. A., Franx M., Fabricant D., 2001, ApJ, 551, 825
- Jones D. H., Bland-Hawthorn J., 2001, ApJ, 550, 593
- Kennicutt R. C., 1992, ApJ, 388, 310
- Kennicutt R. C., 1998, ARA&A, 36, 189 (K98)
- Le Fèvre O., Crampton D., Lilly S. J., Hammer F., Tresse L., 1995, ApJ, 455, 60
- Le Fèvre O. et al., 2001, in Proceedings of the Conference “Deep Fields”, ed. S. Cristiani, A. Renzini, R.E. Williams, Astrophysics Symposia Series-Springer, p. 236
- Lilly S. J., Tresse L., Hammer F., Crampton D., Le Fèvre O., 1995, ApJ, 455, 108
- Lilly S. J., Le Fèvre O., Hammer F., Crampton D., 1996, ApJ, 460, L1
- Lin H., Yee H. K. C., Carlberg R. G., Morris S. L., Sawicki M., Patton D. R., Wirth G., Shepherd C. W., 1999, ApJ, 518, 533
- Madau P., Ferguson H. C., Dickinson M. E., Giavalisco M., Steidel C. C., Fruchter A., 1996, MNRAS, 283, 1388
- Moorwood A. et al., 1999, ESO Messenger, No. 95
- Moorwood A. F. M., van der Werf P. P., Cuby J. G., Oliva E., 2000, A&A, 362, 9
- Osterbrock D. E., 1989, Astrophysics of Gaseous Nebulae and Active Galactic Nuclei, Univ. Sci. Books
- Pascual S., Gallego J., Aragón-Salamanca A., Zamorano J., 2001, A&A, 379, 798
- Pei Y. C., 1992, ApJ, 395, 130
- Pickles A. J., 1998, PASP, 110, 863
- Schade D., Lilly S. J., Crampton D., Hammer F., Le Fèvre O., Tresse L., 1995, ApJ, 451, L1
- Schechter P., 1976, ApJ, 203, 297
- Seaton M. J., 1979, MNRAS, 187, 73
- Singleton C., 2001, PhD thesis, Univ. of Nottingham
- Steidel C. C., Giavalisco M., Pettini M., Dickinson M., Adelberber K. L., 1996, ApJ, 462, L17
- Sullivan M., Treyer M. A., Ellis R. S., Bridges T. J., Milliard B., Donas J., 2000, MNRAS, 312, 442
- Sullivan M., Mobasher B., Chan B., Cram L., Ellis R., Treyer M., Hopkins A., 2001, ApJ, 558, 72
- Tresse L., Maddox S. J., 1998, ApJ, 495, 691
- Tresse L., Rola C., Hammer F., Stasińska G., Le Fèvre O., Lilly S. J., Crampton D., 1996, MNRAS, 281, 847
- Tresse L., Maddox S. J., Loveday J., Singleton C., 1999, MNRAS, 310, 262
- Yan L., McCarthy P. J., Freudling W., Teplitz H. I., Malumuth E. M., Weymann R. J., Malkan M. A., 1999, ApJ, 519, 47L
- Wang B., Heckman T., 1996, ApJ, 457, 645

This paper has been produced using the Royal Astronomical Society/Blackwell Science L^AT_EX style file.